ChemElectroChem

Research Article
doi.org/10.1002/celc.202500220

Chemistry Europe
European Chemical Societies Publishing

www.chemelectrochem.org

Partially Exfoliated and Oxidized V_2CT_x MXene as a Beneficial Support for the Oxygen Evolution Reaction

Bastian Schmiedecke, Bing Wu, Thorsten Schultz, Norbert Koch, Zdenek Sofer, and Michelle P. Browne*

The oxygen evolution reaction (OER) is a critical bottleneck in water-splitting technologies. Hence, developing efficient and stable OER electrocatalysts is one of the key parameters to improve this technology. Recently, MXenes such as $Ti_3C_2T_x$ and V_2CT_x have shown promise as OER-enhancing additives when combined with transition metal oxides. However, MXene synthesis requires energy-intensive processes, and the materials are prone to oxidation in various environments, such as air, or during electrochemical reactions. While this oxidation is typically considered detrimental, this study investigates whether partially exfoliated and oxidized V_2CT_x can maintain or even enhance OER performance, potentially simplifying the synthesis requirements for V_2CT_x. In this study, V_2CT_x is intentionally oxidized and incorporated into CuCo-based composites at various loadings. X-ray diffraction and X-ray photoelectron spectroscopy confirm the presence of vanadium oxide species in the partially exfoliated and oxidized V_2CT_x. The electrochemical investigations reveal that the partially exfoliated and oxidized V_2CT_x enhances the OER performance compared to fresh V_2CT_x. These findings suggest that, unlike $Ti_3C_2T_x$, partially exfoliated and oxidized V_2CT_x retains its functionality in OER catalysis and even outperforms its fresh counterpart, providing a more accessible and efficient platform for water-splitting applications.

1. Introduction

The world is currently experiencing a climate crisis that is partly caused by the release of CO_2 emissions from fossil fuel-based sources (e.g., petrol, diesel, or coal) utilized for energy applications, such as automotive and aviation industries. To mitigate CO_2 emissions related to the energy sector, renewable energy systems must be further researched and advanced.

Electrochemical water splitting, when coupled with wind turbines or photovoltaics, produces green H_2 that can be used in a fuel cell to produce electricity for various sectors including transportation and construction.[1] In electrochemical water splitting, the H_2 is produced on the cathode, however, it is the reaction on the anode, the oxygen evolution reaction (OER), that hinders the overall reaction.[2] Therefore, if the overpotential and stability of the current state-of-the-art metal oxide catalysts for OER could be improved, then green H_2 production efficiency could be significantly enhanced.

In recent years, the number of publications based on MXene materials combined with metal oxides for the OER in alkaline media has significantly increased.[3] The theoretical rationale for combining MXenes and metal oxides for the OER stems from the fact that current state-of-the-art materials, metal oxides, often suffer from poor electrical conductivity and hydrophilicity. MXene materials are 2D materials made from the delamination and exfoliation of MAX phases most commonly in a hydrofluoric acid-based environment when the targeted application is for the OER.[4] MXene materials hold great promise as a catalyst for the OER due to the ability to tune their conductivity and hydrophilicity through O^-, OH^-, and/or F^- termination sites plus the loading of metal oxides on the termination sites. However, these termination sites can also oxidize under OER conditions and can lead to the breakdown of the aforementioned optimal MXene properties for the OER.[5]

The most common MXene in combination with metal oxides used for many electrochemical applications, including OER, is $Ti_3C_2T_x$.[6] This specific MXene, when oxidized, will transform into TiO_2, which is not only an inactive OER material but also possesses insulating properties.[5] Hence, it will cause the overall film to lose a significant amount of conductivity and OER activity. Kaplan et al. have previously shown that altering the synthesis technique of

B. Schmiedecke, M. P. Browne
Helmholtz Young Investigator Group Electrocatalysis: Synthesis to Devices
Helmholtz-Zentrum Berlin für Materialien und Energie GmbH
Albert-Einstein-Str., 15, 12489 Berlin, Germany
E-mail: Michelle.browne@helmholtz-berlin.de

B. Wu, Z. Sofer
Department of Inorganic Chemistry
University of Chemistry and Technology Prague
Technická 5, 16628 Prague 6, Czech Republic

T. Schultz, N. Koch
Helmholtz-Zentrum Berlin für Materialien und Energie GmbH
14109 Berlin, Germany

T. Schultz, N. Koch
Institut für Physik & CSMB
Humboldt-Universität zu Berlin
12489 Berlin, Germany

Supporting information for this article is available on the WWW under https://doi.org/10.1002/celc.202500220

the metal oxide/MXene, e.g., physically mixed or chemically functionalized, can influence the OER.[4] The chemically functionalized composite had improved OER activity compared to a physically mixed Co-$Ti_3C_2T_X$ presumably due to the physically mixed composite having increased free $Ti_3C_2T_x$ sites available for oxidation when in contact with the electrolyte. The oxidation of $Ti_3C_2T_x$ MXenes (partially or fully) during the OER is likely, which will result in an insulating material being formed, and this will lead to a decline in the OER activity. However, there are other MXene materials that, when oxidized, could be valuable for the OER, e.g., V_2CT_x oxidizing to vanadium oxide.

It has been shown that vanadium oxides improve the OER activity of other metal oxides when combined. Recent experimental validation of V_2CT_x's promising performance has been provided by Kaplan et al. [7] who demonstrated that $Co_{0.66}Fe_{0.34}$ layered double hydroxides supported on V_2CT_x MXenes are more stable than $Ti_3C_2T_x$-based analogs for OER applications.[4] Their systematic investigation revealed that vacancy-engineered $V_{1.8}CT_x$ composites achieved exceptional performance with overpotentials as low as 304 mV at 10 mA cm^{-2}, while maintaining excellent stability under practical anion exchange membrane electrolyzer conditions. Xu and coworkers have reported that a $CoVO_x$ material outperforms pure CoO_x and VO_x for the OER in alkaline electrolyte, which they correlated to optimum M–OH bond strength from the typical volcano plot.[8] However, by utilizing the V_2CT_x MXene as the precursor to the VO_x materials, various properties of the MXene may remain in the bulk of the catalyst, which still promotes the OER. Hence, the conductive and hydrophilic nature of the MXene may still contribute to the oxidized MXene/metal oxide composites. Furthermore, V_2CT_x is comparatively harder and takes longer to synthesize compared to $Ti_3C_2T_x$. This results in the partial presence of the V_2AlC MAX phase still present even after three days of MXene synthesis.[9] Hence, if partially exfoliated V_2CT_x could be an efficient OER catalyst, the need for full exfoliation of this MXene would not be required, which would shorten the synthesis procedure.

To evaluate whether oxidized and partially exfoliated V_2CT_x can enhance the OER, this study intentionally oxidizes partially exfoliated V_2CT_x and combines it with CuCo to assess its impact on the catalytic performance. These composites are further compared to fresh V_2CT_x/CuCo composites recently reported by our group, aiming to determine whether the oxidized V_2CT_x MXene remains beneficial for OER electrocatalysis or shares the degradation behavior observed for $Ti_3C_2T_x$ when oxidized during the OER.[10]

2. Results and Discussion

2.1. Structural Characterization

In this study, partially exfoliated V_2CT_x was prepared using an in situ HF method by adding NaF and HCl to a Teflon container with V_2AlC at 90 °C for three days, **Figure 1**A. Three days of synthesis was chosen due to literature reports that show that the MAX phase is still present after this period.[9] The partly exfoliated V_2CT_x was then left in a vial to naturally oxidize in air for six

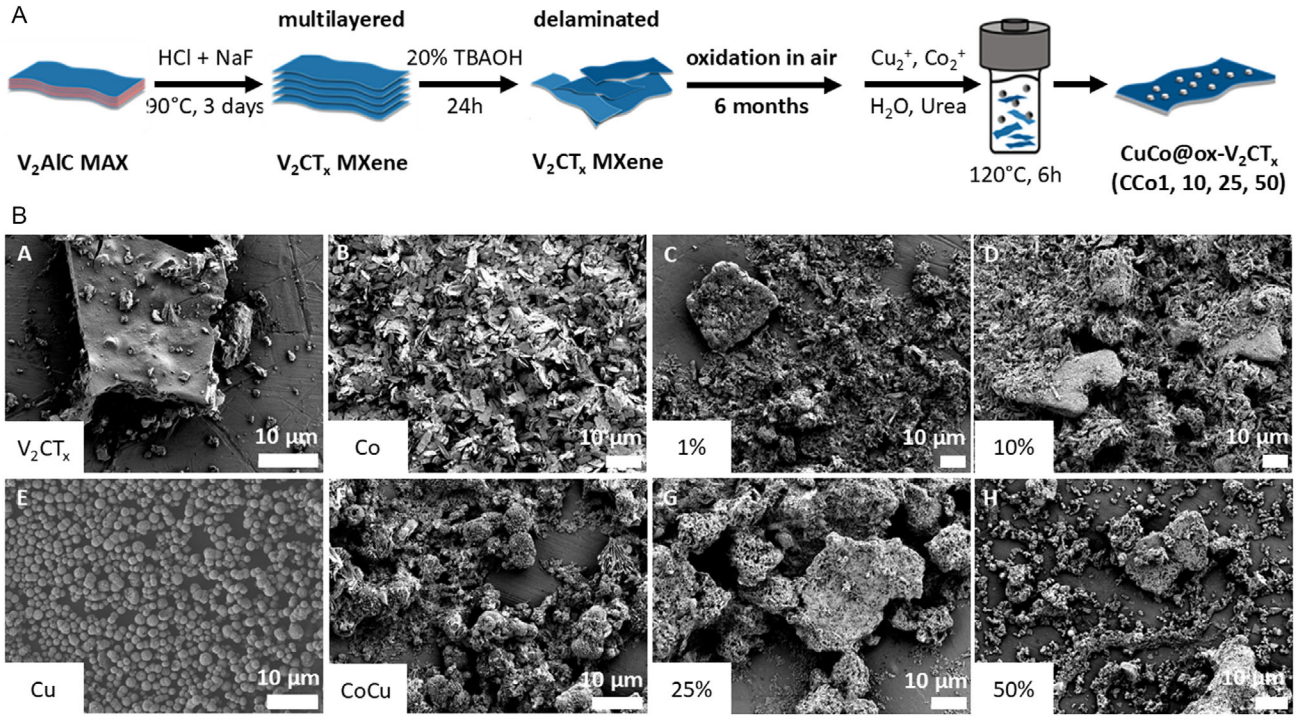

Figure 1. A) Schematic of the preparation of the ox-V_2CT_x and the CuCo hydroxides. B) Scanning electron microscopy images of (A) pure oxidized V_2CT, (B) pure Co, (C) CCo1, (D) CCo10, (E) pure Cu, (F) pure CuCo, (G) CCo25, and (H) CCo50.

months. The oxidation was conducted under ambient laboratory conditions (20–25 °C, 40–60% relative humidity). This oxidized and partially exfoliated V_2CT_x will be denoted as ox-V_2CT_x.

After six months, the ox-V_2CT_x was used to synthesize CuCo/ox-V_2CT_x composites by a hydrothermal method previously reported to make CuCo/fresh V_2CT_x composites for the OER, which will be used as comparative benchmarks to assess whether ox-V_2CT_x is a beneficial material for the same reaction.[10] Briefly, as shown in Figure 1A, the ox-V_2CT_x, urea, Co and Cu salts were added to a hydrothermal vessel, stirred and then heated to 120 °C for 6 h. For this study, four composite materials were synthesized, 1%, 10%, 25%, and 50% ox-V_2CT_x (CCo1, CCo10, CCo25, and CCo50) to allow for the direct comparison with the fresh V_2CT_x previously reported for the OER.[10]

The ox-V_2CT_x, metal oxides and the hybrid materials were subjected to scanning electron microscopy (SEM) to determine the various morphologies formed during the hydrothermal process, as presented in Figure 1B and Figure S1, Supporting Information (higher magnification). The pure V_2CT_x exhibits flake-like morphology with smaller particles. The flake-like morphology is consistent with nonoxidized V_2CT_x; however, the particle structures would suggest the oxidation of the V_2CT_x. The pure Cu material has a sphere-like morphology, and the pure Co material exhibits a coarse flake morphology. The pure CuCo material shows particle aggregation, which from our previous study on this CuCo material consists of flake and rod particles. The CuCo/ox-V_2CT_x composite materials all exhibit aggregated particle morphologies, with CuCo covering the MXene sheets in a uniform fashion, similar to the CuCo/fresh V_2CT_x composites previously reported. To evaluate the elemental distribution and compositional uniformity of the hybrid materials, EDS elemental mapping was performed. The EDS maps shown in Figure S3, Supporting Information, reveal uniform distribution of vanadium, copper, and cobalt across all CCo@V_2CT_x samples (Figure S3C–F, Supporting Information), confirming successful integration of CuCo with the V_2CT_x MXene framework. Vanadium signals are consistently detected throughout all mapped regions, providing direct evidence of the underlying MXene substrate presence. Copper and cobalt generally exhibit homogeneous spatial distribution across the catalyst surface, indicating effective coverage of the MXene substrate. Notably, some localized copper agglomeration is observed, particularly at the edges of MXene flakes. The uniform elemental distribution confirmed by EDS mapping validates the formation of well-integrated hybrid materials, supporting the successful synthesis strategy employed for the CCo electrocatalyst series.

The ox-V_2CT_x and CuCo composite materials alongside the composite materials underwent characterization by X-ray diffraction (XRD) to determine the bulk crystal structure of the catalysts. **Figure 2**A compares the XRD patterns of the MAX phase, fresh/partially exfoliated V_2CT_x and ox-V_2CT_x to evaluate the structural transformations induced by the MXene oxidation. The XRD pattern of the fresh V_2CT_x displayed a prominent reflection at 7.4° corresponding to the (002) reflection of the V_2CT_x MXene. The peaks at 13.53° and 41.3° indicate that the material is not fully exfoliated and contains residual MAX phase, suggesting that the etching process was incomplete, leaving behind unconverted V_2AlC. In contrast, the XRD pattern of the ox-V_2CT_x exhibited a significantly less intense and shifted (002) reflection at 9.1°, indicating that a portion of the MXene structure remains and restacking has occurred (the peak at 9.1° in Figure 2A is highlighted with a *). Several peaks observed in the ox-V_2CT_x pattern correspond to vanadium oxide phases. Reflections at 20.31°, 25.58°, 27.15°, and 31.13° match well with the V_2O_5 phase (JCPDS no. 41–1426), suggesting the formation of vanadium pentoxide as a primary oxidation product. Peaks at 21.5° and 30.69° may be attributed to V_4O_9 (JCPDS no. 71–2248). The ox-V_2CT_{xx} also revealed prominent reflections at 13.49° and 41.21°, which are a typical characteristic of the MAX phase (V_2AlC). However, this peak is more intense when compared to the fresh MXene XRD, hence this peak could be the combination of two XRD reflections. The 13.49° may also correspond to the (002) reflection of the MXene, shifted to a higher 2θ value, which would indicate further restacking of the MXene or changes in interlayer spacing upon oxidation.

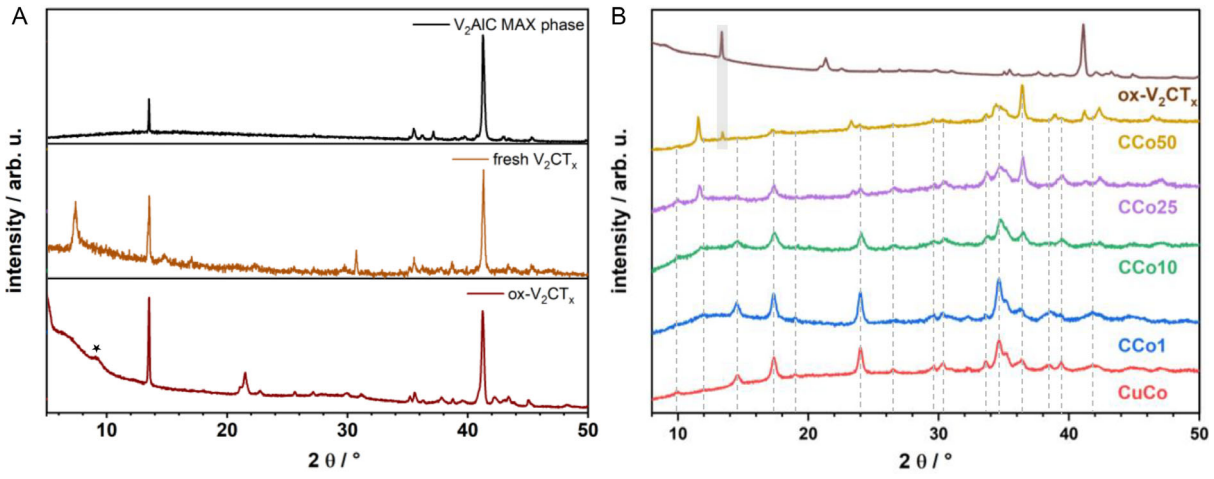

Figure 2. A) X-ray diffraction (XRD) pattern of pure partially exfoliated and oxidized V_2CT_x, V_2AlC MAX phase, and fresh V_2CT_x. B) XRD pattern of pure CuCo and CuCo/ox-V_2CT_x composites.

Hence, the (002) reflection of the MXene may split into two peaks, which has been previously observed by Wu and coworkers upon heating V_2CT_x.[11]

As shown in Figure S2, Supporting Information, the pure Co and pure CuCo materials are indexed to cobalt carbonate hydroxide (ICDD: 04-024−2162, Figure S2, Supporting Information) and Kolwezite (ICDD: 00-029−1416, Figure S2, Supporting Information) phases, respectively, consistent with previous findings.[10] As these phases already have been discussed in prior work, detailed spectra are included in the SI and discussion in our previous work.[10] The CCo1 to CCo50 composite materials were analyzed by XRD to examine the structural evolution as increasing amounts of ox-V_2CT_x were introduced, Figure 2B. The diffractograms of these composites are notably similar to those observed in the previously studied CC1 to CC50 compounds. A prominent peak at 11.5°, observed in the CCo50 composite, aligns with the shifting of the V_2CT_x (002) reflection observed in our previous study, suggesting V_2CT_x MXene is still present in the bulk of the material and restacking of the MXenes occurs after the hydrothermal synthesis due to the bonding with the CuCo. In addition, several key trends were observed in the diffraction patterns with increasing ox-V_2CT_x content. A peak at 14.5° gradually decreases in intensity as more ox-MXene is added, eventually vanishing for CCo50. Similar trends were observed for peaks at 17.5°, 19°, and 24°, a decrease in intensity with increasing MXene addition, indicating a diminishing contribution from the original carbonate hydroxide phases in the composite. Furthermore, various peaks increase in intensity with more ox-MXene. Notably, a peak at 36.3° becomes more pronounced and intense, suggesting a change in the CuCo structure due to the increasing contribution from the MXene. Additionally, the (002) peak from the stacked MXene in the ox-V_2CT_x sample, Figure 2A, emerges at 13.4° in the CCo50 composite. This peak is absent in the other composite materials, due to the lower amount of ox-V_2CT_x in these composites.

X-Ray photoelectron spectroscopy (XPS) was carried out to determine the surface oxidation states of the pure ox-V_2CT_x, the CuCo, and the CuCo/V_2CT_x composite materials (**Figure 3**). The C1s and V2p high resolution regions for the ox-V_2CT_x material (left in air for six months) reveal that the MXene surface has been completely oxidized. The V–C bond in the C1*s* region, typically observed at ≈282 eV in fresh V_2CT_x due to the carbide bond between vanadium and carbon atoms in the MXene structure, is completely absent in the ox-V_2CT_x material. This disappearance confirms surface oxidation of the V_2CT_x. The V2*p* region exhibits a V2$p_{3/2}$ peak at 517 eV, which is indicative of V^{4+} or V^{5+}, in agreement with XRD results.

The Cu2*p* and Co2*p* high resolution XPS regions for the mixed CuCo oxide show that Cu and Co are both present in an oxidation state of +2, most likely as hydroxides (Figure 3A).[12] Addition of 1% V_2CT_X to the mixed CuCo material leads to the emergence of a new peak at about 2.5 eV lower binding energy and therefore to a partial reduction of the Cu^{2+} to Cu^{1+} or metallic Cu (Cu^0).[13] Interestingly, with increasing V_2CT_x, content the amount of Cu^{1+}/Cu^0 increases. This reduction in the Cu core level was also observed with increasing amount of fresh V_2CT_x, however, the

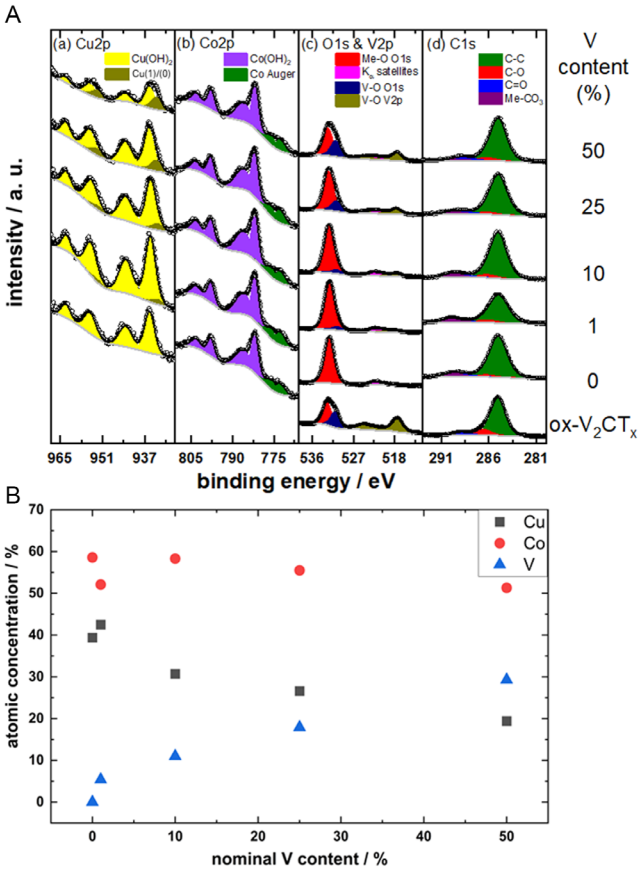

Figure 3. A) High resolution XPS Cu2*p*, Co2*p*, O1*s*, V2*p*, and C1*s* core levels of the pure oxidized V_2CT_x, mixed CuCo, and CuCo/ox-V_2CT_x composites and B) surface atomic concentrations of Cu, Co, and V in the pure CuCo and CuCo/ox-V_2CT_x composites.

ratio of the Cu^{2+} to the Cu^{1+}/Cu^0 was lower when the V_2CT_x was fresh.[10] The oxidation state of cobalt in the CuCo stayed unchanged with addition of V_2CT_x.

From the high-resolution core levels in Figure 3A, the surface atomic concentrations of the Co, Cu, and V in the mixed CuCo and CuCo/oxidized V_2CT_x composites were calculated and are illustrated in Figure 3B. The compositional analysis reveals systematic changes. With the addition of 1% ox-V_2CT_x, the atomic concentration of Co decreases while the Cu increases, which would ultimately result in a catalytic surface that is further enriched with Cu compared to the pure CuCo material. Furthermore, for the 10% oxidized composites, the Co increases to its original mixed CuCo value, while the Cu significantly decreases to about 30 at%. For the 25% oxidized composite, the Cu again significantly decreases to 25% and even further for the 50% oxidized composite to about 20 at%. For these two composites (25% and 50%), the cobalt at% at the surface decreased with further V_2CT_x addition. This resulted in the 50% composite exhibiting the same surface Co at% as the 1% composite. However, for the 50% composite the surface has more V at% and less Cu at% than its composite counterparts.

For water splitting applications hydrophilic surfaces could be beneficial, because they enhance the wettability of the catalyst surface, which could improve the electrode surface interaction

with the aqueous electrolyte.[10] The hydrophilicity of the catalysts in this work was assessed through contact angle measurements, as illustrated in **Figure 4**. The contact angle of the unmodified CuCo showed 145°, indicative of its hydrophobic nature. Upon introducing 1% V_2CT_x, the contact angle exhibited a slight decrease of only 1°, suggesting minimal impact on the surface wettability. However, as the content of the oxidized MXene is increased, the contact angle continues to decrease, reaching 140° for CCo10, 135° for CCo25, and 123° for CCo50. It is noteworthy that when fresh V_2CT_x is incorporated into CuCo, the contact angle decreases more drastically (from 150° for CuCo to 38.9° for CC50) compared to when oxidized V_2CT_x MXene is used,[10] suggesting that the surface chemistry and oxidation state of the MXene play a crucial role in modulating the surface wettability.

2.2. Electrochemical Characterization

The electrochemical behavior of pure CuCo, pure ox-V_2CT_x, and the four CuCo/ox-V_2CT_x hybrid materials (CCo1, CCo10, CCo25, and CCo50) was evaluated toward OER in 1 M NaOH. **Figure 5**A represents the cyclic voltammetry (CV) response of the investigated materials conducted at a scan rate of 40 mV s^{-1} to elucidate their redox properties. The cyclic voltammograms for the CuCo and CuCo/ox-V_2CT_x composite materials show characteristic redox peaks corresponding to the oxidation of cobalt and copper, confirming the presence and activity of both metals in the OER process. For the CuCo sample, the first oxidation peak (A1) appears at 1.09 V versus reversible hydrogen electrode (RHE), which can be attributed to the Co(II) to Co(III) redox transition.[14] For the CCo1 to CCo50 materials, this peak shifts slightly toward lower potentials compared to the pure CuCo, Figure 5A. The complex oxidation region around 1.40–1.44 V versus RHE contains overlapping redox transitions (A2-A4) involving Cu, Co, and V species. Peak A2 (at ~1.40 V vs. RHE) likely corresponds to the Co(III) to Co(IV) redox transition, and A3 (at ≈1.42 V vs. RHE) to the Cu(I) to Cu(II) transition.[14] Then A4 can be related to the oxidation of V(IV) to V(V), which can be observed around 1.43 V versus RHE, according to the vanadium Pourbaix diagram.[15] In the CuCo/ox-V_2CT_x composite samples, the intensity of the A2–A4 peaks increases with increasing ox-V_2CT_x content until CCo25. The peak for CCo50 at 1.44 V versus RHE is slightly less intense compared to CCo25. These results suggest that the oxidized MXene continues to enhance the redox activity of the metals.

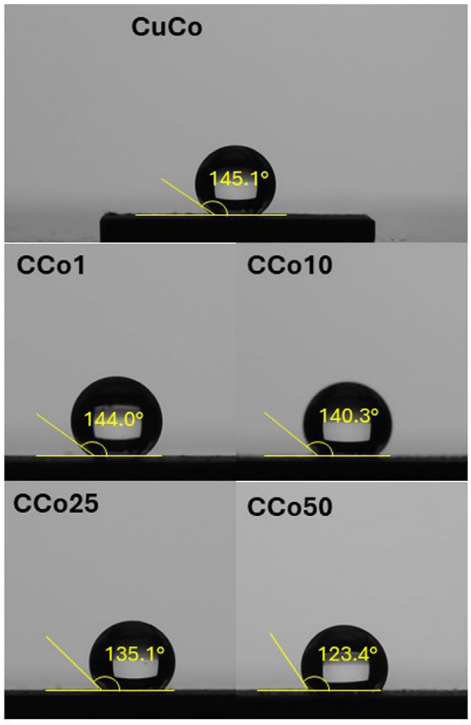

Figure 4. Contact angle measurements of CCo compounds and the pure CuCo.

This enhancement may be attributed to several factors, including increased availability of vanadium centers at the surface due to the oxidation and the exposure of higher surface area. However, it is important to note that in this study, the V_2CT_x was oxidized, forming various vanadium oxide species, which differs from the fresh V_2CT_x used in the previous study.[10] This oxidation leads to changes in the composite material's electrochemical behavior. Unlike fresh V_2CT_x, which is more conductive and capable of directly contributing to enhanced electron transport, oxidized vanadium species in the structure of the MXene may result in lower conductivity, disrupting the carbide network. On the other hand, they provide new redox-active sites that could influence catalytic activity. Indeed, the comparison between the hybrid materials evaluated in this study containing oxidized V_2CT_x, and the materials with fresh V_2CT_x from the last study clearly shows that the materials with fresh V_2CT_x generate more charge from the CVs, than the materials with oxidized V_2CT_x. These results indicate that it could be important to maintain the MXene's state to fully leverage their conductive properties for better OER performance.

The double layer capacitance (C_{dl}) values were extracted from the CVs to quantify the electrochemically active surface area (ECSA), presented in **Table 1**. Larger C_{dl} values reflect an increased ECSA, indicating more accessible active sites for the OER,[16] thus influencing the catalytic performance. The ECSA was calculated using the formula

$$\mathrm{ECSA} = \frac{C_{dl}}{C_s} \quad (1)$$

where C_s is the specific capacitance of the catalyst surface, typically assumed to be in the range of 20, 40, and 80 μF cm^{-2} for metal oxides in alkaline media.[17,18] These values are used as benchmarks to standardize ECSA calculations, accounting for the variability in specific capacitance observed in different metal oxide catalysts. Although C_s is assumed to be constant within these ranges, it may vary slightly depending on material morphology or surface properties. Reporting ECSA values for multiple C_s benchmarks captures this variability and allows for more consistent comparison with literature data. We chose to report

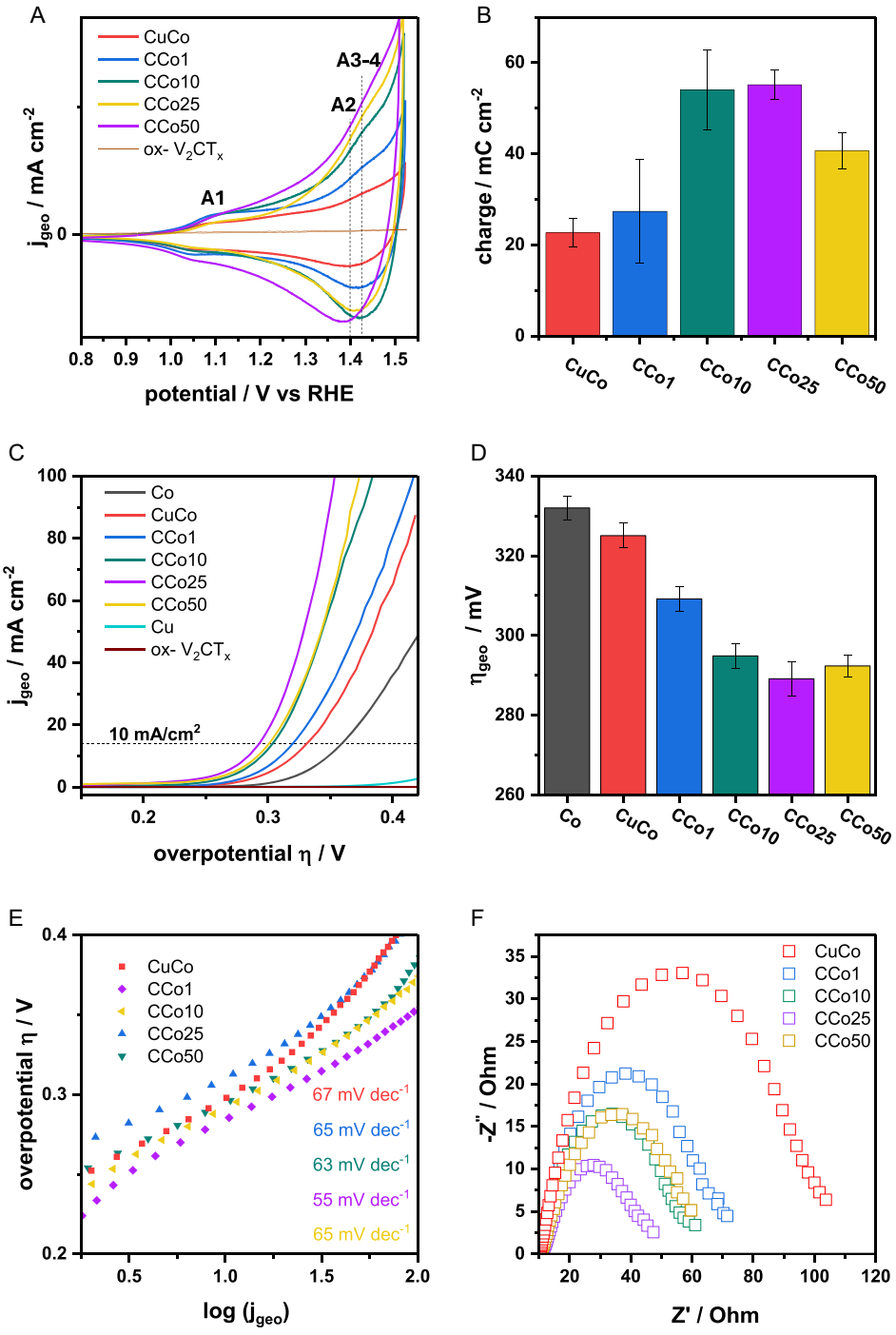

Figure 5. A) Cyclic voltammograms of the pure ox-V_2CT_x material, pure CuCo, and the CuCo/ox-V_2CT_x composites recorded at a scan rate of 40 mV s^{-1} in 1 M NaOH. B) Corresponding charge values in mC cm^{-2} for the anodic sweep. C) Linear sweep voltammogram profiles of the prepared materials in 1 M NaOH. D) Corresponding overpotentials at 10 mA cm^{-2}. E) Corresponding Tafel slopes. F) Corresponding Nyquist plots in OER region.

and discuss C_{dl} values rather than solely ECSA because C_{dl} directly reflects the electrochemical behavior of the material. This approach ensures that the comparison remains meaningful when variations in specific capacitance occur. By combining C_{dl} values with normalized ECSA estimates, a more comprehensive understanding of active site availability and catalyst performance is provided.

For the pure CuCo composite, a C_{dl} value of 11.3 mF cm^{-2} was measured. The introduction of ox-V_2CT_x into the CuCo system led to an increase in the C_{dl}. For CCo1, the C_{dl} value increased from 11.3 to 13.7 mF cm^{-2}, demonstrating a slight positive effect. The CCo10 composite exhibited an increase in C_{dl} to 25.4 mF cm^{-2}, highlighting a greater improvement in the accessible surface area. This suggests that the integration of ox-V_2CT_x enhances

Table 1. Double layer capacitance (C_{dl}) and corresponding ECSA values of pure CuCo and the CCo composites.

Material	CdI [μF cm^{-2}]	ECSA [cm^2] (cs = 20 μF)	ECSA [cm^2] (cs = 40 μF)	ECSA [cm^2] (cs = 80 μF)
CuCo	11.3 ± 3.2	0.57 ± 0.16	0.28 ± 0.08	0.14 ± 0.04
CCo1	13.7 ± 5.7	0.69 ± 0.28	0.34 ± 0.14	0.17 ± 0.07
CCo10	25.4 ± 2.0	1.27 ± 0.10	0.64 ± 0.05	0.32 ± 0.03
CCo25	27.6 ± 1.6	1.38 ± 0.08	0.69 ± 0.04	0.35 ± 0.02
CCo50	20.3 ± 2.0	1.02 ± 0.10	0.51 ± 0.05	0.25 ± 0.03

the dispersion of active sites and promotes more efficient electron transfer. The highest C_{dl} value was observed for the CCo25 composite, with a measured value of 27.6 mF cm^{-2}. This composite seems to have achieved the best balance between ox-V_2CT_x content and surface area exposure, leading to maximum active site availability. However, the C_{dl} value for CCo50 dropped to 20.3 mF cm^{-2}, suggesting that an excessive amount of ox-V_2CT_x can hinder the overall electrochemical performance. This reduction in surface area is likely due to agglomeration, which may block access to some of the active sites and limit the effectiveness of the catalyst. While the redox peaks are still present, the overall activity is slightly reduced compared to the CCo25 composite, indicating that careful optimization of the ox-V_2CT_x content is essential for maximizing the OER performance. In conclusion, the CV and C_{dl} analysis clearly show that the addition of ox-V_2CT_x to CuCo-based catalysts enhances the electrochemical surface area and charge transfer properties. The optimal ox-V_2CT_x loading in this study, as demonstrated in the CCo25 composite, leads to the highest C_{dl} and the best OER performance, which will be discussed in the following paragraph. However, excessive ox-V_2CT_x content can reduce accessibility to active sites, emphasizing the importance of tuning the composition for optimal catalytic activity.

To analyze the OER performance of the materials in this study, linear sweep voltammetry (LSV) was performed, with the results presented in Figure 5C. The pure copper as well as the pure ox-V_2CT_x exhibit negligible OER activity from the LSVs. This result for the ox-V_2CT_x is different from the result for the fresh V_2CT_x which exhibited an overpotential of 422 mV, indicating that the oxidation of this pure MXene leads to a more inactive material toward the OER. The pure Co and the pure CuCo material exhibit overpotentials of 332 ± 3 and 325 ± 3 mV, respectively, showing that an addition of copper is beneficial in this system for the OER. Interestingly, even a small addition of ox-V_2CT_x, in the composite CCo1, lowered the overpotential at 10 mA cm^{-2} to 309 ± 3 mV. With increasing ox-V_2CT_x content, a progressive enhancement in OER activity is observed. The CCo25 material demonstrated the optimal balance, achieving the lowest overpotential of 289 ± 4 mV, indicating that this composition provided the highest efficiency for the OER within this series. However, a further decrease in activity for the CCo50 was observed, with an overpotential of 292 ± 3 mV, suggesting that excess ox-V_2CT_x may lead to site-blocking or possible agglomeration, limiting accessibility to active sites. To evaluate the competitiveness of our CCo25 composite, we compared its performance against established noble metal benchmarks under similar rotating disk electrode (RDE) conditions from the literature (Table S1, Supporting Information). The CCo25 material demonstrates superior performance compared to commercial IrO_2 catalysts, which typically require overpotentials of 300–400 mV at 10 mA cm^{-2} in alkaline media.[19]

To further understand the kinetics of the reaction and examine the correlation between applied potential and current response, the Tafel slopes for the CuCo hybrid materials were analyzed, as shown in Figure 5E. The Tafel slope values exhibit a notable trend, where the addition of ox-V_2CT_x decreases the Tafel slope in the composites. CCo25 exhibits the lowest Tafel slope of 55 mV dec^{-1}, indicating the most favorable kinetics among the composites, likely due to an optimal balance of active sites and improved electronic interaction. On the other hand, the CCo1, CCo10, and CCo50 materials show higher Tafel slopes of 65, 63, and 65 mV dec^{-1}, respectively. These results suggest that while all ox-V_2CT_x additions improve the catalyst's OER kinetics compared to pure CuCo, CCo25 achieves a balance that most effectively supports rapid charge transfer. Furthermore, as the Tafel slope of the pure CuCo and the MXene composite materials were all in the range of 60 mV dec^{-1}. This suggests that the rate determining step (RDS) involves a chemical step after the first electron transfer during the OER.[14] It indicates that the electrochemical adsorption of hydroxide ions is followed by a slower chemical step, likely the formation of O–O bonds.

The Nyquist plot illustrated in Figure 5F presents the charge transfer behavior of the various catalysts during the OER at 1.6 V versus RHE. Among the tested materials, CCo25 demonstrates the lowest charge transfer resistance with 35.3 Ω, suggesting superior electron transfer capabilities at the electrode–electrode interface, which correlates with the observed enhanced catalytic activity in the OER region, Figure 5C. CCo50 and CCo10 show comparable R_{ct} values of 43.8 and 47.1 Ω, respectively, indicating similar charge transfer kinetics between these two samples. The notably higher R_{ct} of pure CuCo in particular shows the importance of compositional modifications, such as in the CCo series, in facilitating more efficient charge transfer during the OER. Overall, these electrochemical impedance spectroscopy (EIS) measurements indicate that the incorporation of varying amounts of oxidized vanadium carbide significantly influences the electron transfer properties, with CCo25 emerging as the most effective catalyst in the OER region. A table with the reported values can be found in the SI (Table S2, Supporting Information).

For the application of catalysts in a real electrolyzer device, the stability under continuous operation is an important parameter to assess. To evaluate the stability and durability of the catalysts, chronopotentiometry was carried out at a current density of 10 mA cm^{-2} for 12 h in 1 M NaOH at RT, **Figure 6**, and the values after operation were compared with initial values from the LSV measurements, Figure 6B. After 12 h of continuous operation, the CCo25 exhibits the lowest overpotential of 270 mV, Table S2, Supporting Information, which is an improvement over its initial overpotential of 289 ± 4 mV. Interestingly, all investigated materials exhibit a decrease in overpotential after the stability

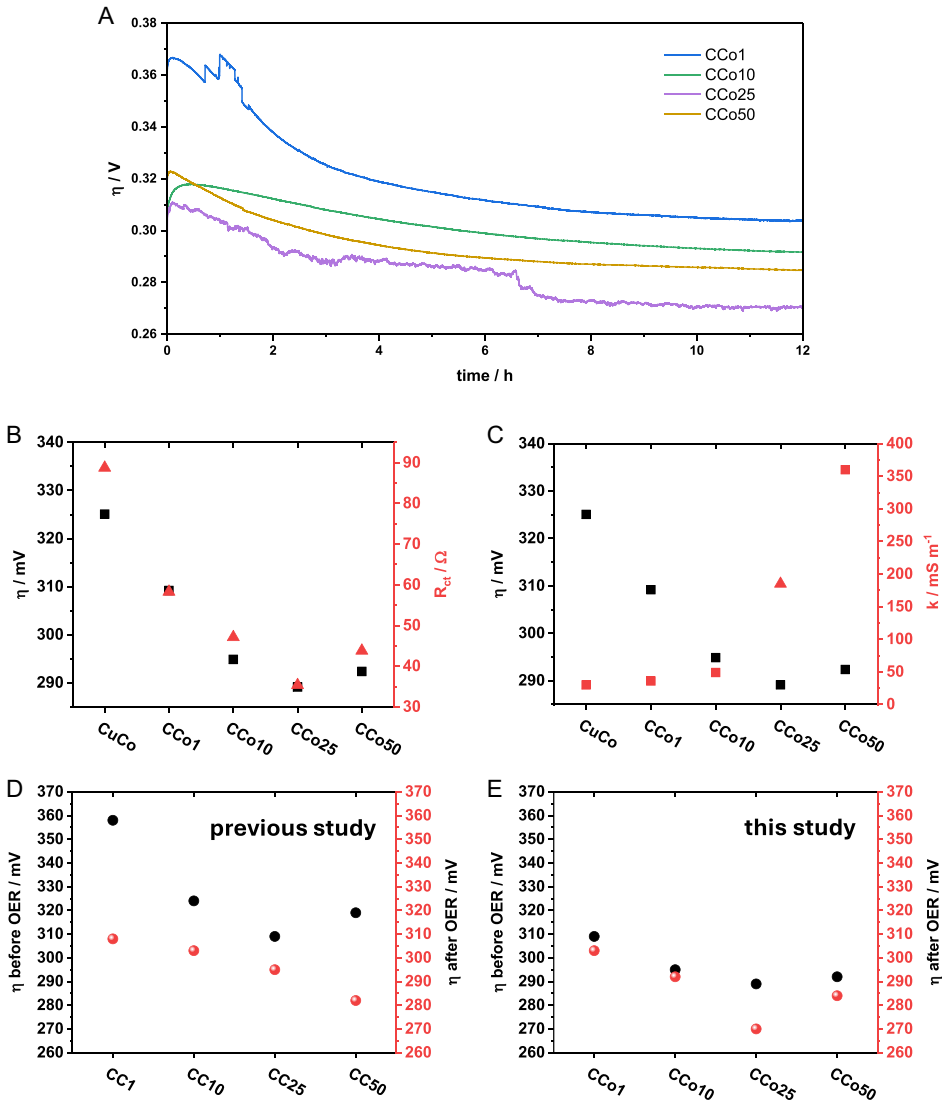

Figure 6. A) Stability performance of the CCo materials at 10 mA cm^{-2} over 12 h. B) Overpotential at 10 mA in comparison to the plotted charge transfer values (R_{ct}). C) Overpotential at 10 mA in comparison to the measured conductivity values. D) Comparison of the overpotential values at 10 mA cm^{-2} before and after the OER for the composite materials of the previous study (CC materials). E) Comparison of the overpotential values at 10 mA cm^{-2} before and after the OER for the composite materials of this study (CCo materials).

test, Table S2, Supporting Information, a similar trend as in the previous study, which was determined to be a result of the preferential leaching of the vanadium over the CuCo, i.e., the OER active sites. To further evaluate the long-term stability of the best-performing material, CCo25 was subjected to extended chronopotentiometry testing over 24 h (Figure S4, Supporting Information). The results revealed again a performance enhancement during prolonged operation. Minor current fluctuations were observed during the test, likely attributed to bubble formation and detachment during sustained high-activity operation. This extended stability test demonstrates promising durability of the CCo25 material.

To elucidate the fundamental origins for the enhanced performance of the CCo25, the charge transfer resistances during OER and the conductivity of the films were determined, Figure 6B–C. The pure copper cobalt hydroxide film shows the lowest conductivity among the catalysts reaching 30 µS m^{-1}, which aligns with its previously observed high charge transfer resistance and lower OER activity, Figure 6B–C; Table S2, Supporting Information. The poor electron transport limits efficiency as electrons are not efficiently transferred to the catalytic sites. This low conductivity is likely a significant factor contributing to the slower electron transfer. The slight increase in conductivity from CuCo to CCo1 (36 µS m^{-1}) may play a role in the minor improvement in electron transfer capabilities. However, this small increase is not substantial enough to have a significant impact on OER performance.

CCo10 exhibits a more noticeable increase in conductivity with 49 µS m^{-1}, while CCo25 shows a significant enhancement, reaching 185 µS m^{-1}. CCo25's higher conductivity would greatly increase the flow of electrons in the catalyst layer, which adds to the various factors that make this material the most active in this

study, which is also observed in the lower charge transfer resistances during OER. CCo50 shows the highest conductivity of 360 μS m^{-1} (Table S4, Supporting Information) and lowest R_{ct} value (Table S2, Supporting Information). However, while high conductivity is beneficial, the overall catalytic performance also depends on other factors such as the surface area, active site accessibility, and material stability. The fact that CCo25 performs better than CCo50 suggests that there might be an optimal balance of all these factors, combined with the redox chemistry of the metal centers of the system.

To gain deeper insights into the fundamental origins of these electrochemical phenomena and the observed optimal performance of CCo25, further XPS analysis was performed, which reveals the underlying compositional and electronic changes that drive the enhanced catalytic activity. The compositional changes detected by XPS (Figure 3B) are statistically significant and directly correlate with the observed electrochemical trends. The addition of 1% ox-V_2CT_x (CCo1) results in a decrease in surface Co content (from ≈58% to ≈53%) and a corresponding increase in Cu content (from ≈39% to ≈42%), which coincides with the improved overpotential from 325 ± 3 mV (pure CuCo) to 309 ± 3 mV and a modest conductivity increase from 30 to 36 μS m^{-1}. However, as the ox-V_2CT_x content increases further, a systematic decrease in surface Cu accessibility occurs. The optimal CCo25 composition, which exhibits the best overall performance (lowest overpotential of 289 ± 4 mV, optimal kinetics with 55 mV dec^{-1} Tafel slope, lowest Rct of 35.3 Ω, and high conductivity of 185 μS m^{-1}), corresponds to a surface with ≈55% Co, ≈27% Cu, and ≈18% V content. This suggests an optimal Cu/Co/V ratio that maximizes OER activity by balancing active site availability with electronic conductivity enhancement.

Additionally, the XPS data reveals the partial reduction of Cu^{2+} to Cu^{1+}/Cu^0 upon ox-V_2CT_x addition (Figure 3A), creates a heterogeneous Cu oxidation state environment that seems to facilitate electron transfer during OER. Furthermore, the progressive increase in V content correlates systematically with conductivity enhancement, demonstrating that ox-V_2CT_x modulates the Cu/Co surface composition and significantly improves electronic conductivity. However, excessive V content (CCo50:≈29 at% V) leads to decreased Cu accessibility (≈20 at% Cu), and while this results in the highest conductivity (360 μS m^{-1}), it slightly reduces overall catalytic activity, demonstrating that optimal performance requires a balanced composition where V enhances conductivity without excessively blocking active sites. Furthermore, the preferential leaching of vanadium observed during stability testing supports the XPS findings, as the V component serves primarily as a conductivity enhancer while the Cu–Co phases remain as the primary active sites for sustained OER activity.

In order to be able to compare the CCo materials to the fresh V_2CT_x composites, Figure 6D and Table S5, Supporting Information presents data from the previous study utilizing fresh V_2CT_x in similar CuCo composites.[10] In that study, the initial overpotential values were higher for each composition compared to the oxidized V_2CT_x composites in this work. While the fresh V_2CT_x materials also showed reductions in overpotential after 12h, the final overpotential values, particularly for the CCo25 composite, were still less optimal than those achieved with the oxidized V_2CT_x here, Figure 6D and E. This improvement may be attributed to the increased structural stability and slightly altered surface chemistry in the oxidized V_2CT_x, which appears to facilitate more stable and efficient catalytic performance over extended periods.

In conclusion, the conductivity values of the catalyst films show a clear correlation with their OER performance, and the compositional changes revealed by XPS analysis. When more ox-V_2CT_x is added to the CuCo system, the conductivity increases progressively, which correlates with the increasing V content. However, the performance of CCo50 indicates that beyond a certain point, other material properties, like active site distribution and material morphology, become more dominant factors. The XPS analysis reveals that while CCo50 achieves the highest conductivity (360 μS m^{-1}) due to its high V content, it also suffers from reduced Cu accessibility (≈20 at% Cu compared to ≈27% for CCo25), which limits the availability of active sites for OER. This demonstrates that optimal catalytic performance requires a delicate balance: sufficient ox-V_2CT_x content to enhance electronic conductivity and create beneficial Cu^{1+}/Cu^0 species, while maintaining adequate Cu surface concentration for sustained catalytic activity. The CCo25 composition achieves this optimal balance, combining high conductivity (185 μS m^{-1}), favorable Cu/Co surface ratio (≈27% Cu and ≈56% Co), and excellent charge transfer properties, ultimately resulting in the best overall OER performance.

2.3. Investigation of Electrochemical Transformation in CCo25 during OER

Operando Raman spectroscopy of the CCo25 hybrid material conducted over the potential range of 0–0.7 V versus Hg/HgO in 1 M NaOH reveals complex electrochemical transformations during OER conditions. Ex situ reference measurements (Figure S5, Supporting Information) enable precise peak deconvolution, identifying distinct vibrational contributions from the active (Cu^{2+}, Co)$(CO_3)(OH)_2$ mixed carbonate hydroxide phase, V_2CT_x MXene support, and Nafion ionomer binder. However, from the large overlap of peaks, it is difficult to determine the state of the CuCo and MXene species but the spectra stay consistent over the potential range until 0.7 V versus Hg/HgO, where most of the peaks under 1000 cm^{-1} disappear which could be due to leaching or bubble interference.

Complementary postmortem XPS analysis reveals structural and chemical changes in the CCo25 catalyst. Most notably, vanadium signals are completely absent in the post-OER spectra, confirming the progressive leaching of vanadium species during electrochemical operation, consistent with our operando Raman observations.[7] Changes in the Cu2*p* and Co2*p* spectral regions indicate surface reconstruction during OER conditions. While direct binding energy comparisons are not possible due to charging effects during measurement acquisition, the spectral changes suggest partial oxidation of both copper and cobalt centers, consistent with the formation of active oxyhydroxide

phases.[20] The complete vanadium dissolution supports our proposed mechanism where V_2CT_x acts as sacrificial modifier that facilitates initial surface reconstruction, leaving behind the active CuCo oxyhydroxide phases. This comprehensive analysis demonstrates that the hybrid material undergoes simultaneous active phase reconstruction (mixed carbonate hydroxide → oxyhydroxide), support degradation (V_2CT_x leaching), and metal oxidation.

3. Conclusion

This study demonstrates that partially exfoliated and oxidized V_2CT_x enhances the OER performance of CuCo-based hydroxides. The optimal material CCo25 achieved a low overpotential of 289 mV at 10 mA cm^{-2}, enhanced conductivity (185 vs. 30 μS m^{-1} for pure carbonate hydroxide), a Tafel slope of 55 mV dec^{-1}, and 24 h stability with continued performance improvement over time. EIS further confirmed the superior charge transfer properties of CCo25, which exhibited the lowest charge transfer resistance during the OER (35.3 Ω) among the composites.

Compositional optimization revealed critical balance effects in the hybrid system. While pure ox-V_2CT_x showed negligible OER activity, its incorporation into the carbonate hydroxide matrix led to significant improvements, with CCo25 emerging as optimal. Excessive V_2CT_x content (CCo50) resulted in reduced performance despite higher conductivity, indicating that the beneficial electronic modification must be balanced against increased MXene degradation. The 25 wt% loading represents the optimal compromise between enhanced charge transfer and acceptable vanadium leaching rates. Chronopotentiometry testing showed remarkable performance enhancement during operation, with overpotential decreasing from 289 to 270 mV after 12 h and extended 24 h testing demonstrating promising durability. The performance enhancement over time could be attributed to progressive surface reconstruction from the mixed carbonate hydroxide precursor to oxyhydroxide phases, as confirmed by postmortem XPS analysis (**Figure 7**B).

Operando Raman spectroscopy combined with ex situ XPS analysis revealed the fundamental mechanisms underlying this exceptional performance. The enhanced activity stems from a complex electrochemical transformation: initial V_2CT_x-mediated reduction of Cu^{2+} to electron-rich Cu^{1+} species, followed by potential-driven surface reconstruction of the $(Cu^{2+},Co)(CO_3)(OH)_2$ precursor to catalytically active phases, and concurrent vanadium dissolution through formation of soluble vanadate species under alkaline OER conditions.

These findings fundamentally redefine the role of V_2CT_x in carbonate hydroxide composites through a comprehensive understanding derived from structural, surface, and electrochemical characterization. Rather than serving as a stable conductive support, the MXene functions as a sacrificial precursor-modifier that enhances electronic conductivity, facilitates surface reconstruction to active phases before undergoing systematic

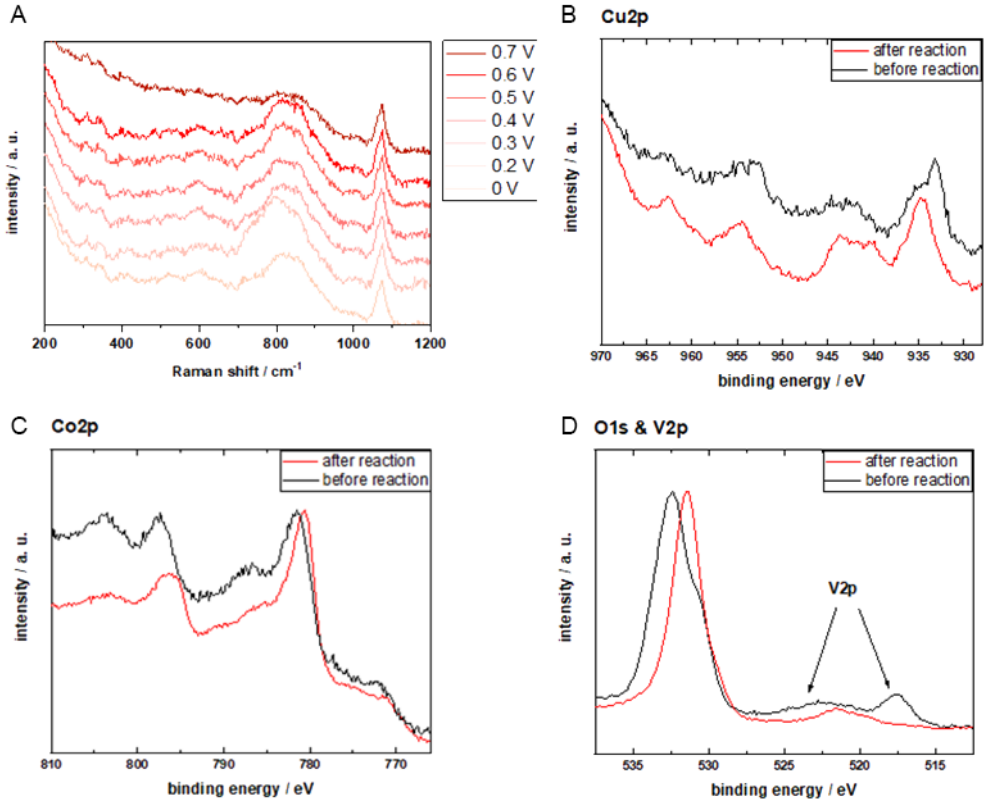

Figure 7. A) In situ Raman spectroscopy of CCo25 from 0 V versus Hg/HgO to 0.7 V versus Hg/HgO in 1 M NaOH. B–D) XPS spectra of CCo25 before and after OER. B) Cu2*p* region. C) Co2*p* region. D) O1*s* & V2*p* region.

degradation during operation. This explains both the enhanced initial performance and the continued improvement during operation, demonstrating that controlled surface reconstruction, not MXene oxidation, drives the OER activity enhancement. The partially exfoliated and oxidized V_2CT_x offers synthetic advantages over fresh MXene, including reduced processing time and equivalent electrochemical benefits, while establishing a new strategy for creating high-performance OER electrocatalysts through designed precursor modification. However, the discovered vanadium leaching phenomenon necessitates validation of MXene stability in practical membrane electrode assemblies under actual electrolyzer operating conditions. This work establishes partially oxidized V_2CT_x as a promising platform for advanced OER applications.

4. Experimental Section

Materials

Sodium hydroxide pellets (≥98%, reagent-grade), isopropanol (≥99%, reagent-grade), ethanol (≥99%, reagent-grade), $Cu(CH_3COO)_2 \cdot H_2O$ (≥99% metal basis, M of 199.65 g mol^{-1}), $Co(CH_3COO)_2 \cdot 4\ H_2O$ (≥99% metal basis, M of 249.08 g mol^{-1}), Tetra-*n*-butylammonium hydroxide (TBAOH, 40% in H_2O), Nafion (5 wt %) and urea (≥99 %, ACS reagent, M of 60.06 g mol^{-1}) were purchased from Sigma–Aldrich. A graphite rod and a mercury–mercury oxide electrode (Hg/HgO) were purchased from redox.me. Sodium fluoride (NaF) and hydrochloric acid (37%, ACS reagent) were purchased from Lachner. Vanadium aluminum carbide MAX phase (V_2AlC) was purchased from Jinzhou Haixin Metal Materials, China. Deionized water (resistivity of 18.2 MΩ cm) was produced using a laboratory system (Barnstead Smart2Pure 3 UV, ThermoFisher Scientific). Alumina paste was purchased from Buehler and glassy carbon disc electrodes with a diameter of 3 mm were purchased from ALS Instruments.

Preparation of Ox-V_2CT_x

To prepare ox-V_2CT_x MXene, the Al layer from its corresponding MAX phase V_2AlC was removed using a mixed HCl and NaF etching solution. The detailed experimental procedure is described as follows: 4.5 g of NaF was stirred and dissolved in 60 mL of distilled water, followed by the slow addition of 60 mL of concentrated HCl. Then, 5 g of V_2AlC MAX phase was added to the solution slowly, in a timeframe of 10 min, and stirred for 1 h in an atmospheric environment until no bubbles were observed. The mixture was then transferred to a stainless-steel autoclave with a Teflon liner, sealed, and continuously stirred in an oil bath for three days at 90 °C. The solid product from the first etching cycle was subjected to the same etching steps again. The product was then centrifuged three times with DI water to obtain the etched precursor. Subsequently, to exfoliate the precursor, it was stirred in 20 mL of 20% TBAOH solution for 24 h and then diluted with DI water to reach a 100 mL suspension, that was stirred for another 24 h. To remove residual TBAOH the suspension was centrifuged at 10,000 rpm and then washed three times with an ethanol/water solution (1:4). Finally, to remove any unetched MAX phase or other impurities, centrifugation at 1000 rpm was performed. This process yielded well-exfoliated V_2CT_x MXene powder for further use, which was then left in ambient laboratory air (20–25 °C, 40%–60% relative humidity) to naturally oxidize for six months.

Preparation of the Pure Cu, Co, and CuCo and Composite Materials

All hybrid materials, as well as the pure materials without oxidized MXene, were synthesized utilizing a urea-assisted hydrothermal route. The following experimental procedure was employed: V_2CT_x MXene powder was dispersed in 30 mL ultrapure water for 10 min in an ultrasonic bath. Then, 5 mmol urea, 1 mmol $Cu(CH_3COO)_2 \cdot H_2O$, and 2 mmol $Co(CH_3COO)_2 \cdot 4\ H_2O$ were added to the solution, and it was stirred for 30 min to fully dissolve the compounds. Subsequently, the solution was transferred to a Teflon liner, sealed in a stainless-steel autoclave and then heated to 120 °C where it was kept for 6 h to undergo hydrothermal treatment. The mixture was allowed to cool down to room temperature after this treatment. The precipitate was collected using centrifugation at 5000 rpm for 10 min and then washed with DI water first and ethanol second, three times each. The sediment was collected and dried at 60 °C for 10 h. The dried powder samples were labeled as CCo1, CCo10, CCo25, and CCo50 (for 1, 10, 25, and 50 wt% MXene content, respectively). Additionally, the pure metal and mixed-metal compounds were prepared utilizing the same hydrothermal route without the V_2CT_x MXene and were labeled pure Co, pure Cu, and pure CuCo.

Scanning Electron Microscopy and Energy Dispersive X-Ray Spectroscopy

The morphological characteristics and elemental composition of the as-prepared samples were investigated using a Karl Zeiss MERLIN field emission scanning electron microscope (FE-SEM) equipped with an Oxford Ultim Extreme energy-dispersive X-ray spectroscopy (EDX) system. The instrument operates with an accelerating voltage range of 20 V to 30 kV, providing high-resolution imaging capabilities with 1.4 nm resolution at 1 kV. Secondary electron imaging was performed using the SE2 detector. Elemental mapping and qualitative compositional analysis were performed at 3.5 keV accelerating voltage using the integrated EDX system to determine the spatial distribution and atomic ratios of constituent elements within the catalyst materials.

Contact Angle Measurements

The contact angles of the materials were recorded on spray-coated catalyst films (on 1 × 2 cm silicon substrates), utilizing an Ossila Contact Angle Goniometer (Model T2001A5) with a high-resolution camera 1920 × 1080, equipped with a monochromatic light source for accurate edge detection. The system used a 25 µl glass syringe with a blunt needle (0.47 mm diameter) for precise droplet dispensing. Analysis and determination of the contact angles was performed with the software from Ossila Contact Angle software, which employs Canny edge algorithm and polynomial curve fitting for droplets above 10° contact angle. The measurements accuracy was ±1° over a range of 5° to 180°.

Conductivity Measurements

Conductivity measurements were performed on catalyst films, prepared by spray-coating a catalyst ink (1:1 DI water/isopropanol mixture) onto 1 × 2 cm silicon substrates. The measurements were carried out using an Ossila Four-Point Probe (Model T2001A4) equipped with soft contact probes to prevent damage to the catalyst films. The system utilized gold-plated, spring-loaded probes with rounded tips (0.24 mm radius) that apply a uniform force of 60 g to ensure good electrical contact without damaging the sample

surface. Data acquisition and analysis were performed using the Ossila Sheet Resistance Lite software.

X-Ray Diffraction

The phase analysis of the samples was performed at room temperature (RT) by powder XRD utilizing a Bruker D8 ADVANCE powder diffractometer with Cu-K**α** radiation of 40 kV and a beam current of 40 mA (λ(Cu-K**α**1) = 0.1541 nm and λ(Cu-K**α**2) = 0.1544 nm. Diffraction patterns were collected between 3.5° and 80° applying a step size of 0.015°.

Photoelectron Spectroscopy

XPS measurements were conducted using a JEOL JPS-9030 setup with a base pressure of 2.10^{-9} mbar. The powders were evenly distributed on carbon tape for the measurements. A nonmonochromatic Al K**α** source with 300 W power was used for excitation and a hemispherical analyzer with a pass energy of 50 eV (surveys) and 20 eV (narrow scans) was used to detect the emitted photoelectrons. The binding energy scale of the analyzer was calibrated by setting the Au4$f_{7/2}$ and the Cu2$p_{3/2}$ peaks of clean gold and copper foils to 84.0 and 932.6 eV, respectively. However, since the samples showed charging, we shifted the binding energy of the C–C peak of the carbon tape to 285.0 eV for comparison. CasaXPS was used to fit the spectra.[21]

Electrochemical Measurements

In this study, a conventional three-electrode setup was utilized to examine the electrochemical properties of the prepared materials. All measurements were performed at RT in nitrogen saturated 1 M NaOH solution, freshly prepared from NaOH pellets. A mercury/mercury oxide (Hg/HgO) electrode acted as the reference, and a graphite rod served as the counter electrode. A glassy carbon (GC) disk with a diameter of 3 mm was used to prepare the working electrodes. First, the GC disk was polished with alumina paste and then cleaned in water with ultrasonic waves for 5 min. Then, the working electrode was prepared as follows: 10 mg catalyst powder was ultrasonically dispersed in a solution consisting of 496 µl DI water, 496 µl isopropanol, and 8 µl Nafion to form a homogenous ink. Subsequently, 11.3 µl of the ink was drop-cast onto the polished GC disk to reach a catalyst loading of 1.6 mg cm^{-2} and allowed to dry in air at room temperature. The electrochemical cell was connected to a PalmSens4 workstation and a rotating ring disc electrode (RRDE, ALS-Japan).

Before the electrochemical tests, each electrocatalyst was conditioned by running ten CV cycles at a scan rate of 40 mVs^{-1} in a potential range of −0.2 to 0.6 V versus Hg/HgO. Polarization and Tafel profiles were acquired in a potential range of 0–0.85 V versus Hg/HgO with a scan rate of 1 $mV\ s^{-1}$ while rotating the working electrode at 1600 rpm. EIS were performed in a nonfaradaic region over a frequency range of 1 Hz to 1 MHz with a 10 mV perturbation to determine the resistance of the cell. Additionally, EIS was conducted in the OER region at 1.6 V versus RHE in the range of 1 kHz to 100 kHz with an oscillation amplitude of 10 mV, to assess the charge transfer resistance of the materials under operation. The electrochemical double layer capacitance (C_{dl}) was evaluated by recording CVs at various scan rates (2 to 150 $mV\ s^{-1}$) within a 100 mV potential window in the nonfaradaic region. The ECSA was estimated using three different specific capacitance values of 20, 40, and 80 µF cm^{-2}.[17] The stability of the electrocatalysts during operation was tested utilizing chronopotentiometry at a constant current density of 10 mA cm^{-2} for 12 h.

Operando Raman

Operando Raman spectroscopic investigations were conducted using an i-Raman Plus portable spectrometer equipped with a 785 nm laser coupled with a PalmSens electrochemical workstation. The potential-dependent operando Raman measurements utilized a magnetic-mount Raman electrochemical flow cell (Raman ECFC 3.5 cm^2, Redox.me) filled with 4.5 ml of NaOH (1 M) electrolyte solution. The catalyst sample ink (containing 4 wt% Nafion) was deposited onto a gold support substrate through spray coating, serving as the electrical contact for the working electrode. The three-electrode configuration included a platinum wire counter electrode and a mercury/mercury oxide (Hg/HgO) reference electrode. Prior to Raman acquisition, chronoamperometric stabilization was performed for 60 s at each applied potential ranging from 0 to 0.7 V (vs. Hg/HgO).

Acknowledgements

The authors gratefully acknowledge the Helmholtz Association's Initiative and Networking Fund (Helmholtz Young Investigator Group VH-NG-1719) for the funding. M.P.B. greatly acknowledges support from the German Federal Ministry of Education and Research in the framework of the project Catlab (03EW0015A/B). Z.S. was supported by ERC-CZ program (project LL2101) from Ministry of Education Youth and Sports (MEYS). Z.S. was also supported by Czech Science Foundation (GACR no. 23-06702S) and used large infrastructure from project Advanced Functional Nanorobots (reg. no. CZ.02.1.01/0.0/0.0/15_003/0000444 financed by the EFRR).The authors would like to address particular thanks to R. Schwiddessen, M. Tovar, F. Ruske, and K. Schwartzburg from the X-Ray and Microscopy and Spectroscopy Corelabs of the Helmholtz Zentrum Berlin for providing access to their facility and training on the equipment. Open Access funding was enabled and organized by Projekt DEAL.

Conflict of Interest

The authors declare no conflict of interest.

Author Contributions

Bastian Schmiedecke: formal analysis (lead); investigation (lead); methodology (lead); and writing—original draft (lead). **Bing Wu**: methodology (equal); and writing—review & editing (equal). **Thorsten Schultz**: data curation (equal); formal analysis (equal); investigation (equal); and writing—review & editing (equal). **Norbert Koch**: funding acquisition (equal); supervision (equal); and writing—review & editing (equal). **Zdenek Sofer**: funding acquisition (equal); supervision (equal); and writing—review & editing (equal). **Michelle P. Browne**: conceptualization (lead); funding acquisition (lead); investigation (lead); methodology (lead); supervision (lead); and writing—original draft (equal).

Data Availability Statement

The data that support the findings of this study are available from the corresponding author upon reasonable request.

Keywords: metal oxide MXene composites · oxidized MXene · oxygen evolution reaction · V_2CT_x

[1] F. Zeng, C. Mebrahtu, L. Liao, A. K. Beine, R. Palkovits, *J. Energy Chem.* **2022**, *69*, 301.
[2] F. Bao, E. Kemppainen, I. Dorbandt, R. Bors, F. Xi, R. Schlatmann, R. van de Krol, S. Calnan, *ChemElectroChem* **2021**, *8*, 195.
[3] a) J. Chen, X. Gao, J. Li, Z. Kang, J. Bai, T. Wang, Y. Yuan, C. You, Y. Chen, B. Y. Xia, X. Tian, *Electron* **2024**, *2*, e17. b) B. R. Anne, J. Kundu, M. K. Kabiraz, J. Kim, D. Cho, S.-I. Choi, *Adv. Funct. Mater.* **2023**, *33*, 2306100.
[4] C. Kaplan, R. M. Restrepo, T. Schultz, K. Li, V. Nicolosi, N. Koch, M. P. Browne, *Electrochim. Acta* **2024**, *490*, 144269.
[5] D. Tyndall, L. Gannon, L. Hughes, J. Carolan, S. Pinilla, S. Jaśkaniec, D. Spurling, O. Ronan, C. McGuinness, N. McEvoy, V. Nicolosi, M. P. Browne, *npj 2D Mater. Appl.* **2023**, *7*, 15,
[6] a) M. P. Browne, D. Tyndall, V. Nicolosi, *Curr. Opin. Electrochem.* **2022**, *34*, 101021. b) X. Li, Z. Huang, C. E. Shuck, G. Liang, Y. Gogotsi, C. Zhi, *Nat. Rev. Chem.* **2022**, *6*, 389.
[7] C. Kaplan, K. Dharmaraj, T. Schultz, L. Qin, N. Chen, D. A. Douglas-Henry, B. Schmiedecke, M. Buldu-Akturk, A. Zuber, I. Dorbandt, M. Reinhardt, Y. Rodriguez-Ayllon, Y. Lu, V. Nicolosi, N. Koch, J. Rosen, M. P. Browne, *Adv. Funct. Mater.* **2025**, 2503842.
[8] L. Liardet, X. Hu, *Acs Catal.* **2018**, *8*, 644.
[9] a) K. Matthews, T. Zhang, C. E. Shuck, A. VahidMohammadi, Y. Gogotsi, *Chem. Mater.* **2022**, *34*, 499. b) M. Fatima, S. A. Zahra, S. A. Khan, D. Akinwande, J. Minár, S. Rizwan, *Nanomaterials* **2021**, *11*, 1707.
[10] B. Schmiedecke, B. Wu, T. Schultz, A. A. Emerenciano, N. Sharma, D. A. Douglas-Henry, A. Koutsioukis, M. T. Görüryılmaz, V. Nicolosi, T. Petit, N. Koch, Z. Sofer, M. P. Browne, *J. Mater. Chem. A* **2024**, *12*, 24248.
[11] M. Wu, B. Wang, Q. Hu, L. Wang, A. Zhou, *Materials* **2018**, *11*, 2112.
[12] a) M. C. Biesinger, *Surf. Interface Anal.*, **2017**, *49*, 1325. b) J. G. Dillard, M. H. Koppelman, *J. Colloid Interface Sci.* **1982**, *87*, 46.
[13] J. A. Torres-Ochoa, D. Cabrera-German, O. Cortazar-Martinez, M. Bravo-Sanchez, G. Gomez-Sosa, A. Herrera-Gomez, *Appl. Surf. Sci.* **2023**, *622*, 156960.
[14] R. L. Doyle, I. J. Godwin, M. P. Brandon, M. E. G. Lyons, *Phys. Chem. Chem. Phys.* **2013**, *15*, 13737.
[15] M. Lee, X. Ding, S. Banerjee, F. Krause, V. Smirnov, O. Astakhov, T. Merdzhanova, B. Klingebiel, T. Kirchartz, F. Finger, U. Rau, S. Haas, *Adv. Mater. Technol.* **2020**, *5*, 2000592.
[16] a) A. Karmakar, S. Kundu, *Mater. Today Energy* **2023**, *33*, 101259. b) R. Martínez-Hincapié, J. Wegner, M. U. Anwar, A. Raza-Khan, S. Franzka, S. Kleszczynski, V. Čolić, *Electrochim. Acta* **2024**, *476*, 143663.
[17] C. C. L. McCrory, S. Jung, J. C. Peters, T. F. Jaramillo, *J. Am. Chem. Soc.* **2013**, *135*, 16977.
[18] a) M. J. Gira, K. P. Tkacz, J. R. Hampton, *Nano Converg.* **2016**, *3*, 6. b) R. Boggio, A. Carugati, S. Trasatti, *J. Appl. Electrochem.* **1987**, *17*, 828.
[19] J. Li, *Nanomicro. Lett.* **2022**, *14*, 112.
[20] J. Du, C. Li, X. Wang, T. G. J. Jones, H.-P. Liang, *Electrochim. Acta* **2019**, *303*, 231.
[21] N. Fairley, V. Fernandez, M. Richard-Plouet, C. Guillot-Deudon, J. Walton, E. Smith, D. Flahaut, M. Greiner, M. Biesinger, S. Tougaard, D. Morgan, J. Baltrusaitis, *Appl. Surf. Sci. Adv.* **2021**, *5*, 100112.

Manuscript received: June 4, 2025
Revised manuscript received: August 18, 2025
Version of record online: November 3, 2025